High corrosion resistance duplex fcc + hcp cobalt based entropic alloys: An experimental and theoretical investigation

(article starts on next page)
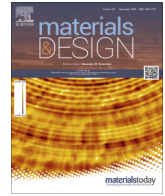
High corrosion resistance duplex fcc + hcp cobalt based entropic alloys: An experimental and theoretical investigation

Wei Wang [a,*], Wangzhong Mu [b,c,*], Dawei Wei [a,d], Hongliu Wu [a], Libo Yu [a], Torbjörn Jonsson [f], Henrik Larsson [c,e,*], Huahai Mao [c,e]

[a] Department of Chemical Engineering, Northeast Electric Power University, Jilin 132012, China
[b] Key Laboratory of Electromagnetic Processing of Materials (Ministry of Education), Northeastern University, Shenyang, China
[c] Department of Materials Science and Engineering, KTH Royal Institute of Technology, SE-100 44 Stockholm, Sweden
[d] Department of Materials Science and Engineering, University of Science and Technology Beijing, 100083 Beijing, China
[e] Thermo-Calc Software, Råsundavägen 18, SE-16767 Solna, Sweden
[f] Department of Chemistry and Chemical Engineering, Chalmers University of Technology, SE-41 296 Gothengurg, Sweden

HIGHLIGHTS

- A series of duplex fcc + hcp Co-based entropic alloys are discovered as a new category of entropic alloys with outstanding mechanical properties.
- CALPHAD-based thermodynamic calculations were performed to facilitate alloy design and to understand corrosion behaviors.
- The kinetics of the electrochemical corrosion for designed alloys in typical aggressive anion Cl⁻ was investigated by electrochemical tests.
- The theoretical calculations are in good agreement with the experimental observations, this provides a new solution for an efficient designing the corrosion resistance entropic alloys.

GRAPHICAL ABSTRACT
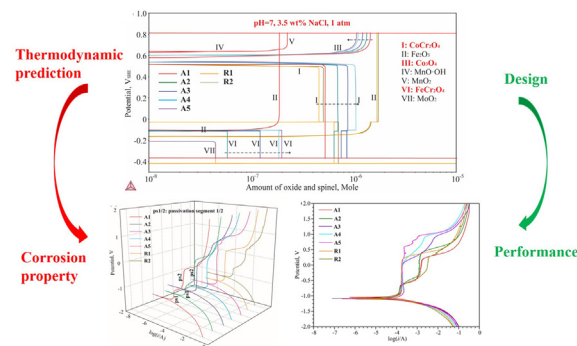
ARTICLE INFO

ABSTRACT

A series of duplex fcc + hcp Co-based entropic alloys are being discovered as a new category of entropic alloys with outstanding mechanical properties, especially to overcome a typical mechanical trade-off between strength and ductility. In this work, CALPHAD-based (CALculation of PHAse Diagram) thermodynamic calculations were performed to facilitate alloy design and to understand corrosion behaviors. The kinetics of the electrochemical corrosion for designed alloys in typical aggressive anion Cl⁻ was investigated by electrochemical tests, including open circuit potential (OCP), polarization and cyclic polarization curves, and electrochemical impedance spectroscopy (EIS). The valence state and the surface morphologies of the passive films were investigated by X-ray photoelectron spectroscopy (XPS) and atomic force microscope (AFM). High corrosion resistance materials with high strength and ductility performances were discovered in the present work. Except for Ni-oxides, various spinel compounds and many other oxides including Co_2O_3, Cr_2O_3, Fe_2O_3, MnO, MoO_3, $CoCr_2O_4$, $FeCr_2O_4$, $CoFe_2O_4$, and $CoMoO_4$ were observed in the passive films. The adsorbed and penetrated corrosive anion Cl⁻ will be prone to breakdown the passive films with less Cr_2O_3, $CoCr_2O_4$ and MoO_3 to form pitting corrosion (also include other localized corrosion, such as intergranular corrosion and crevice corrosion). The

* Corresponding authors at: Department of Materials Science and Engineering, KTH Royal Institute of Technology, SE-100 44 Stockholm, Sweden (W. Mu and H. Larsson).
E-mail addresses: wei6@kth.se (W. Wang), wmu@kth.se (W. Mu), hlarsso@kth.se (H. Larsson).

Nomenclature

Materials (at%)

A1/A2/A3/A4 alloy: $Co_{77.5-x}Cr_xFe_{7.5}Ni_{7.5}Mn_{7.5}$ (x = 15, 20, 25, 30, denoted as A1, A2, A3 and A4, respectively)

A5 alloy: $Co_{46}Cr_{30}Fe_{7.5}Ni_{7.5}Mn_{7.5}Mo_{1.5}$

R1 alloy: $Fe_{67.3}Cr_{18.3}Ni_{12.9}Mo_{1.5}$

R2 alloy: $Fe_{69.4}Cr_{20.2}Ni_{10.4}$

Parameters in electro-chemical investigations

β_c/β_a:	Cathodic/Anodic Tafel slope, mV/dec
$\log i_c/\log i_a$:	Cathodic/Anodic intercept
R_L:	Linear polarization resistance, Ω
E_{corr}:	Corrosion potential, V
i_{corr}:	Corrosion current, μA
$i_{self-corr}$:	Self-corrosion current, μA
E_b:	Breakdown potential, V
i_b:	Breakdown current, μA
E_p:	Passive potential, V
i_p:	Passive current, μA
E_{pro}:	Protection potential, V

$\triangle E_{p-r}$:	E_b-E_p, Passive region, V
$\triangle E_{p-w}$:	E_b-E_{corr}, Passive window, V
f:	Frequency, Hz
φ:	Phase angle, degrees
Z:	Electrochemical impedance, $\Omega \cdot cm^2$
Z':	Real component of impedance, $\Omega \cdot cm^2$
Z'':	Imaginary component of impedance, $\Omega \cdot cm^2$
$|Z|$:	Impedance modulus, $\Omega \cdot cm^2$
R_{bs}:	Resistance of bulk solution, $\Omega \cdot cm^2$
$CPE_{dl,ct}$:	Capacitance of electric double-layer between bulk solution and passive films, F/cm^2
$R_{dl,ct}$:	Charge-transfer resistance of electric double-layer between bulk solution and passive films, $\Omega \cdot cm^2$
$CPE_{pf,ct}$:	Pseudo-double-layer capacitance of passive films, F/cm^2
$R_{pf,ct}$:	Charge-transfer resistance of passive films, $\Omega \cdot cm^2$
R_{pit}:	Resistance of pitting process, $\Omega \cdot cm^2$
$CPE_{pit,ct}$:	Pseudo-double-layer capacitance of pitting process, F/cm^2
$R_{pit,ct}$:	Charge-transfer resistance of pitting process, $\Omega \cdot cm^2$
R_p:	Polarization resistance

microstructure of the hcp martensite with the fcc matrix has played an important role in the propagation of the localized anodic dissolution in the form of cleavage and quasi-cleavage. The theoretical calculations are in good agreement with the experimental observations. This paper paves a way for the future development of high-performance Co-based entropic alloys served in some harsh environments.

1. Introduction

Various cobalt and cobalt–nickel based superalloys are the typical grades for service at elevated temperatures [1–3]. They are widely used in the fields of machining and sophisticated manufacturing industry [4–7], aerospace industry [8,9], and nuclear industry [10–12]. It is known that these alloys have high strength, high corrosion resistance, as well as high wear and galling resistance [13–15].

As an important milestone in materials development, the concept of high entropy alloys [16] (also named multi-principal element alloys (MPEAs) [17,18] or complex concentrated alloys (CCAs) [19]) have changed the design paradigm from conventional based-element corner into the vast multi-component composition space. Cantor HEAs (i.e. CoCrFeNiMn system HEAs) have been extensively studied [16,17,20]. The elements in Cantor HEAs are the most important alloying elements in cobalt/nickel/iron based alloys too, therefore, it is reasonable to say that, there exists a close link between Cantor/Cantor-like HEAs and cobalt/nickel/iron based alloys [21–23].

In recent years, a novel metastable transformation-induced plasticity-assisted high entropy alloy (TRIP-HEA) with dual phases [24] has attracted progressively increasing interest due to its excellent comprehensive properties. Especially this alloy grade is distinguished by balanced strength-ductility properties [25–29]. In our previous work, a new series of duplex Co-based entropic alloys was designed, intermediate to cobalt based alloys and the fcc + hcp duplex TRIP Cantor HEAs [30]. These entropic alloys have produced the thermal-induced hcp phase by homogenizing and quenching to room temperature [31]. The duplex fcc + hcp structure increases the *trans*-grain slip hardening due to a decrease of the thermal stability for the fcc phase at high temperature of

1200 °C. The TRIP effect increases the inter-grain slip hardening due to a decrease of the mechanical stability for the hcp phase at room temperature. Therefore, more strain hardening can be formed which results from the dislocation and transformation induced hardening by the phase transformation fcc → hcp [24,32]. As a summary, dislocation hardening, massive solid solution strengthening, transformation-induced hardening, and many other strengthening mechanisms have played a very significant role in enhancing the comprehensive mechanical properties for duplex TRIP HEAs [33–35].

Besides the high strength and ductility, high corrosion resistance is a prerequisite performance for an advanced engineering material. The equiatomic CoCrFeNiMn HEA is probably the most frequently investigated HEA system. There are studies on the electrochemical corrosion behavior at room temperature [36–38], on the oxidation and deformation mechanisms at elevated temperatures [39,40], and on the radiation-induced segregation mechanisms [41], and so on [42,43]. Using a weak oxidizing acid solution such as dilute sulfuric acid medium (e.g. 0.05 or 0.1 M H_2SO_4) at room temperature, the corrosion resistance of CoCrFeNiMn HEA and 304L stainless steel is similar [36]. The corrosion behaviors of the passivation materials in different oxidizing medium will exhibit complex behaviors due to the typical dual roles between the two factors, i.e. the anodic dissolution/cathodic depolarization behaviors and the anodic passivation behaviors in different concentration acid. For instance, the inhibition efficiency for Al in 0.1 M NaCl decline in the below order: nitrate (NO_3^-) > acetates (Ac^-) > benzonate (Bz^-) > sulphate (SO_4^{2-}) [44]. So SO_4^{2-} also played dual roles on passivation materials as a kind of cathodic depolarizer (like aggressive medium) and anodic passivator (like inhibitor). Until now, besides the reported corrosion resistance HEAs systems, such as Cantor/Cantor-like HEAs [36–38,45] or similar

alloying systems (e.g. CoCrFeNiMo$_x$ (x = 0, 0.2, 0.5, 0.8, 1) [46], low carbon (0, 0.04, 0.11, 0.17 wt% C) CoCrFeNiMn [47], Al$_x$CrFe$_{1.5}$-MnNi$_{0.5}$ [48], Fe$_{40}$Ni$_{20}$Cr$_{20}$Cr$_{20}$ (at.%) [49], etc), more high corrosion resistance HEAs are still need to be found and investigated. Based on the above literature review, it is very significant to develop a series of non-equiatomic CoCrFeNiMn entropy alloys with high corrosion resistance, high strength and ductility performances.

For developing a high corrosion resistance material, passivation and its breakdown in chloride ion (Cl$^-$) solutions is one of the typical and representative criteria, due to the well-investigated "chloride effects" [50–52]. Usually, sodium chloride (NaCl) solution was chosen as the typical aggressive environments. In the present work, the electrochemical corrosion behaviors of a series of duplex fcc + hcp cobalt based TRIP entropic alloys as a continuation of the former developed alloy grades have been investigated [30,31]. Thermodynamic calculations were conducted by using the CAL-PHAD (CALculation of PHAse Diagram) method for facilitating alloy design and predicted corrosion behavior. Electrochemical investigations were also provided to analyze the kinetics of the electrochemical corrosion in typical aggressive anion Cl$^-$. The valence state and the surface morphologies of the passive films were characterized. The current work aims for further developing non-equiatomic duplex HEA with a high corrosion resistance in particular, and the high-performance Co-based alloy to replace Co as binder phases in cemented carbides.

2. Experimental methods

The proposed alloys were prepared using arc melting furnace. High purity raw metallic materials of Co, Cr, Fe, Mn, Ni, and Mo (>99.9 %) were used. The melting was performed in a pure Ar atmosphere. The ingots were turned upside down at least four times in an arc melting furnace, then re-melted in a corundum crucible in a dimension Φ24 mm (outside diameter, O.D.) × 2.5 mm (thickness) × 85 mm (height) in the vacuum induction melting furnace. The melted samples were sealed in evacuated quartz tubes and homogenized at 1200 ℃ for 2 h, then water quenched to room temperature.

The homogenized and quenched samples for the electrochemical tests were cut, ground, and mechanically polished with the dimension of 10 mm × 10 mm × 4.5 mm. The samples were epoxy encapsulated and only left a 10 mm × 10 mm surface, i.e. the standard size for the electrochemical investigation. The exposed surface was selected as the working electrode for the conventional three-electrode electrochemical cell. The working electrode was polished, cleaned with ethanol and distilled water, and dried before each test. The electrochemical tests were performed using CHI760E electrochemical workstation (Shanghai Chenhua Instrument Co., China) with a three-electrode system, i.e. a platinum electrode as the counter electrode, a saturated calomel electrode (i.e. SCE, V_{SCE} = 0.208 V, 3 M KCl) as the reference electrode, and the working electrode. The tests were measured in a 3.5 wt% NaCl solution (pH = 7 ± 0.2) at 298 K. All the standard potentials used in this work are given on the standard hydrogen scale (i.e. SHE).

The electrochemical tests performed in this study include open-circuit potential (OCP), electrochemical impedance spectroscopy (EIS), potentiodynamic polarization, and cyclic potentiodynamic polarization. The OCP was first measured for 3600 s. EIS measurements were conducted with a frequency sweep from 100 kHz to 10 mHz, an amplitude of 0.005 V, and a quiet time of 2 s. The potentiodynamic polarization and cyclic potentio-dynamic polarization were conducted at the potential range from –2.0 V to 2.0 V with a scanning rate of 10 mV·s^{-1}, a quiet time of 2 s, and sensitivity of e^{-1} A/V. At least two parallel tests were performed to ensure reliable results.

The homogenized and quenched samples for the microstructure characterization and composition investigation were dealt with an extra electropolishing process, the details has been described elsewhere [30]. Energy dispersive X-ray spectroscopy (EDS) was performed using a LEO-1450 type scanning electron microscopy (SEM, Zeiss, Germany) equipped with NORAN-7 EDS detector (Thermo Scientific, USA). All the samples were determined using 20 kV for 90 s to obtain a sufficient signal. X-ray diffraction (XRD) was performed using a RINT-TRIII X-ray Diffractometer SmartLab (Rigaku Corporation, Japan) using Cu-K$_\alpha$ (wavelength λ = 1.5406 Å) with a 1D D/txX Ultra high speed and resolution scanning silicon strip detector. The diffraction patterns were recorded from 10° → 90° 2θ with 0.02° scan steps at 40 kV and 150 mA with a 1D D/teX Ultra high-speed silicon strip detector.

The valence analysis of the passive films was measured by X-ray photoelectron spectroscopy (XPS). To obtain stable passive films, the bulk samples were immersed in 3.5 wt% NaCl solution at 298 K for 2 h. Subsequently, the specimens were measured by using a Thermo Scientific ESCALAB 250 Imaging XPS Microprobe with monochromatic Al K$_\alpha$ (hν = 1486.6 eV) X-ray radiation at a pass energy of 20 eV high-resolution spectra. The reference binding energy was set using the standard C1s peak at 284.6 eV. All the peaks were calibrated by the standard C1s perk. The XPS data were analyzed by the commercial Avantage software.

The corroded samples were imaged using a standalone AFM (NT-MDT NTEGRA) operating in semi-contact mode, in the air at room temperature with a relative humidity of 30 %. Silicon probe (NT-MDT HA_NC) was used to capture the surface topography with a scan size as 10 μm × 10 μm, with a typical curvature radius of the tip of 10 nm and a typical resonant frequency of 235 kHz.

3. Computational design strategy

To be one of the most significant methods for changing the conventional trial and error method in materials science, the CALPHAD methodology has developed from the prediction of phase diagrams in the early stage to extend greatly in thermodynamic, kinetic, and precipitation calculations and simulation, etc [53,54]. In this work, CALPHAD predictions were performed to obtain reasonable guidance on alloy design and thermodynamics of electrochemical corrosion. The thermodynamic calculations in the present work were performed by the Thermo-Calc software (Thermo-Calc 2021b version) [55,56] using the thermodynamic and kinetic databases TCAQ3 [57], SSUB5 [58], TCHEA4 [59,60], TCNI11 and MOBNI5 [61,62].

The excellent balancing strength-ductility mechanical properties are the most distinguished trademark for high quality metal structural engineering materials. However, it is always a dilemma to coordinate high strength-ductility synergy materials. In general significance, Cr and Ni are the strong passivated metals in the cobalt/nickel/iron based alloys, for instance, the most famous passivation structural engineering materials being 18/10 and 18/8 stainless steel. In particular, as the most important candidate alloying element in the cobalt/nickel/iron based alloys, chromium play a very significant role in enhancing corrosion resistance. A considerable quantity of compacted Cr$_2$O$_3$ oxide in the passive barrier films may provide a good mechanical isolation effect between the metal substrate and the corrosive medium. To obtain the "stainless" effect in the Fe–Cr binary system, 12 wt% Cr is usually considered to be the critical minimum composition. The value of E_F^0 for the Fe–12Cr (wt.%) alloy is reduced approximately 1 V compared with the value of pure Fe. The regulation for the dissolution rate dependence of the alloying component concentration in the Fe–Cr binary alloys, which was investigated theoretically and experimentally,

was concluded by the Tamman rule (or Tamman's n/8-rule) [63,64].

It was found that, the thermal-induced martensitic transformation may occur in our designed cobalt based alloys (with 0–40 at% Cr) [30]. Therefore, alloys A1–A4 with approximately (15, 20, 25, and 30) at% Cr, and 7.5 at% Fe/Ni/Mn were designed in this work. Furthermore, alloy A5 was designed based on alloy A4 by doping with 1.5 at% Mo (the same Mo content as in alloy R1). Alloys R1

and R2 were chosen as the reference alloys having typical 18/10 and 18/8 stainless steel compositions. The phase transformation and microstructures for the alloys A1–A4 are predicted by thermodynamic calculations. Thermodynamic calculations for designing materials are given in Fig. 1. The calculation results indicated that it is possible to induce the fcc → hcp phase transformation. The nominal and chemical compositions of the proposed alloys are listed in Table 1.
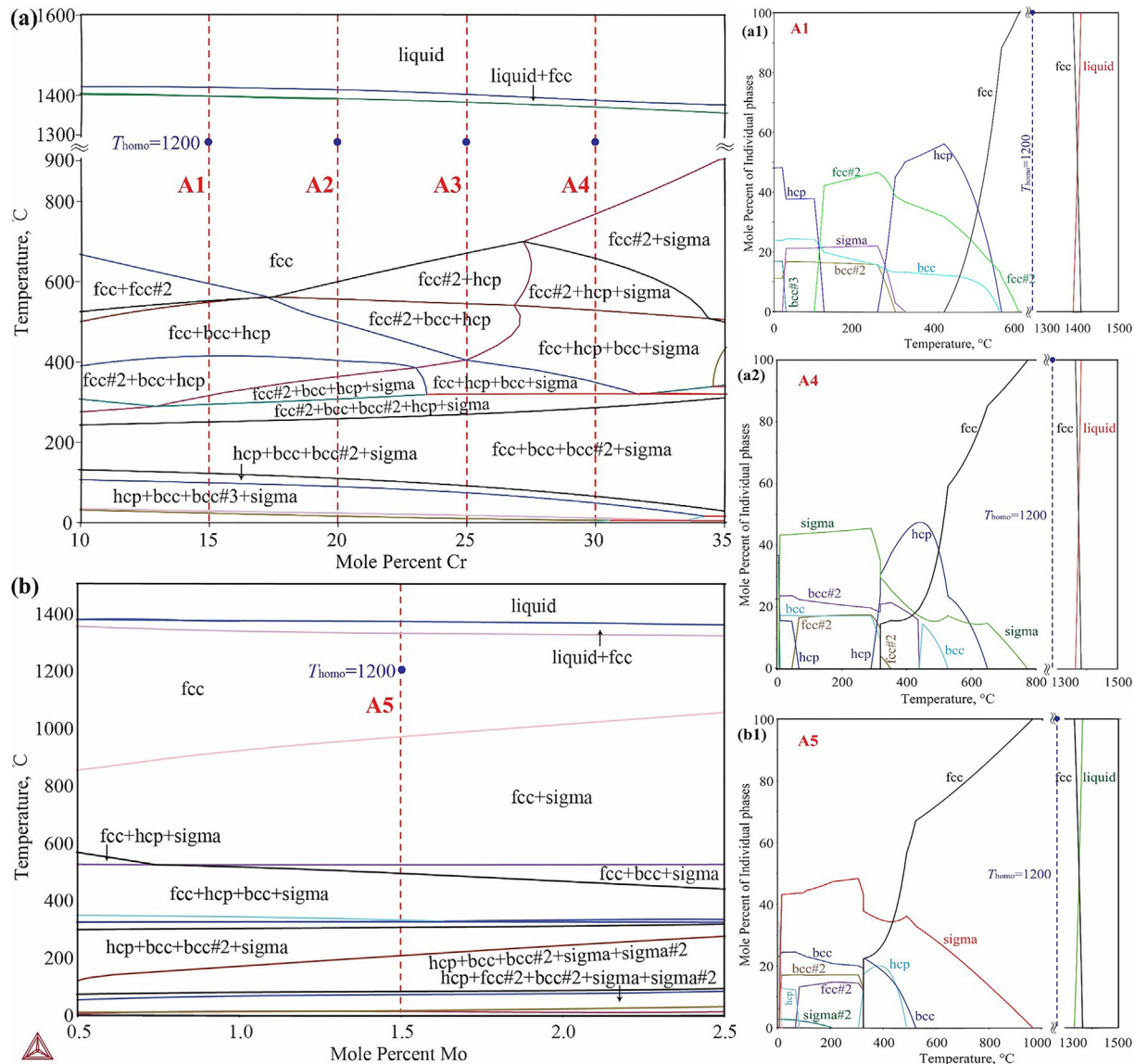

Fig. 1. The CALPHAD-predicted diagram for designing alloys. The isoplethal sections of the Co-Cr-Fe-Ni-Mn system at $x(Fe) = x(Ni) = x(Mn) = 7.5$ at% (a) and the Co-Cr-Fe-Ni-Mn-Mo system at $x(Cr) = 30$ at% and $x(Fe) = x(Ni) = x(Mn) = 7.5$ at% (b). The phase fractions at equilibrium as a function of temperature for alloy A1 (a1), A4 (a2), and A5 (b1).

Table 1
Composition of alloys (at%) obtained by EDS.

Alloy	Co	Cr	Fe	Mn	Ni	Mo	Nominal
A1	60.62	15.18	7.70	7.66	8.84	–	$Co_{62.5}Cr_{15}Mn_{7.5}Fe_{7.5}Ni_{7.5}$
A2	57.00	21.49	7.94	5.36	8.21	–	$Co_{57.5}Cr_{20}Mn_{7.5}Fe_{7.5}Ni_{7.5}$
A3	53.54	25.82	7.66	5.11	7.88	–	$Co_{52.5}Cr_{25}Mn_{7.5}Fe_{7.5}Ni_{7.5}$
A4	46.63	30.83	8.05	6.00	8.51	–	$Co_{47.5}Cr_{30}Mn_{7.5}Fe_{7.5}Ni_{7.5}$
A5	46.15	31.95	7.85	4.67	8.02	1.38	$Co_{46}Cr_{30}Mn_{7.5}Fe_{7.5}Ni_{7.5}Mo_{1.5}$
R1	–	17.45	67.34	–	13.45	1.76	$Fe_{67.3}Cr_{18.3}Ni_{12.9}Mo_{1.5}$
R2	–	20.97	70.55	–	8.48	–	$Fe_{69.4}Cr_{20.2}Ni_{10.4}$

4. Results and discussion

4.1. Thermodynamic calculations for alloy design and electrochemical corrosion

The CALPHAD-predicted phase equilibria of the alloys A1–A5 are shown in Fig. 1. It can be seen that the single-phase region for fcc exists in a wide temperature range below solidus approximately between 700 and 1350 ℃ for the alloys A1–A4. Accordingly, the homogenization temperature can be chosen in this temperature range. The equilibrium phase diagram (Fig. 1) predicts the thermodynamic stable phases. It's worth mentioning that the real microstructure obtained in experiments is a result of non-equilibrium physical and chemical processes. In the designed samples, a thermal-induced martensitic transformation fcc → hcp was formed in the quenching process from homogenized temperature (i.e. 1200 ℃ in the present work) to room temperature. The stabilities of the hcp phase at low temperatures, in Fig. 1, indicate the possibility of martensitic transformation in these alloys. The detailed CALPHAD prediction for the driving force of the martensitic transformation can be found elsewhere [30]. The martensitic transformation was confirmed experimentally in the XRD patterns (see Fig. 2) and other characterization techniques such as electron backscatter diffraction (EBSD), and in-situ real time observation using high temperature confocal laser scanning microscopy in our previous works [30,31].

The CALPHAD-predicted Pourbaix diagram (i.e., potential-pH diagram) for alloy A1 in 3.5 wt% NaCl solution at 1 atm and room temperature is show in Fig. 3. The 3.5 wt% NaCl solution at 298 K is neutral with a pH of 7 ± 0.2. Based on the calculated Pourbaix diagrams for the alloys A1–A4, it is revealed that the stable solid phases in equilibrium with the aqueous solution are the same, but the critical potentials and pH of specific reactions differ slightly. It should be mentioned that the potential in the Pourbaix diagram is the equilibrium potential, while in a real corrosion system the potential represents the non-equilibrium potential. That is, the non-equilibrium potential is obtained from the equilibrium potentials undergoes complex polarization in the real electrochemical corrosion systems. In other words, Pourbaix diagram can provide a kind of interpretation of the thermodynamics for a series of electrochemical reactions in an equilibrium state, but not in a non-equilibrium state. Nevertheless, the calculated Pourbaix diagram is undoubtedly a powerful methodology to predict

the complex species in a series of specific reactions (involving various spinel and other oxides such as $NiFe_2O_4$, $CoCr_2O_4$, $CoFe_2O_4$, $FeCr_2O_4$, MnO_2, Co_3O_4, $MnOOH$, $Co(OH)_2$, and so on). Under certain potential-pH domains in the thermodynamic stable state, and the thermodynamic analysis of the electrochemical corrosion is still an excellent starting point to understand the corrosion mechanisms. In Pourbaix diagram, potential (set as the y-axis) represents the transferred electrons involved in the electrochemical reactions, which also reflects the activation energy of anodic reactions (i.e. oxidation reactions) in the process of metal corrosion. The calculated Pourbaix diagram will be analyzed and discussed with other results in the following sections.

Thermodynamics and kinetics of electrochemical corrosion are the basic and significant factors to design high corrosion-resistant materials. Considering this, electrochemical tests are the typical methods to investigate the kinetics of the corrosion mechanisms, especially for passivation materials.

4.2. Corrosion behaviors under real circumstances

For a high-quality structural material, self-passivation ability is one of the most significant performances. Electrochemical tests are almost the most indispensable and essential techniques for studying corrosion mechanisms. In the passivation period, both $\triangle E_{p-r}$ and $\triangle E_{p-w}$ are two important parameters for estimating the passivation ability, i.e. the more noble of the potential for $\triangle E_{p-r}$ and $\triangle E_{p-w}$, the higher the passivation ability. With the increase of the potential, the passivation materials undergo a transition from a self-passivation state into a transpassivation state, and the parameters E_b and i_b are two significant physical characteristics in the presence of specific aggressive anions (e.g. Cl^-). The results show that based on the 4 electrochemical parameters ($\triangle E_{p-r}$, $\triangle E_{p-w}$, E_b and i_b), the samples can be classified into 3 groups, the normal corrosion resistance samples (alloys A1, A2, and R2 denoted as Group 1 here), the high corrosion resistance samples (alloys A3 and R1 denoted as Group 2) and the super-high corrosion resistance samples (alloys A4 and A5 denoted as Group 3, especially for alloy A5). The classification is based on the analysis from the potentiodynamic polarization curves of the alloys in 3.5 wt% NaCl solution at 1 atm and room temperature (see Fig. 4 and Table 2). For the normal corrosion resistance alloys (Group 1, especially for alloys A1 and A2) with increasing the potential, the polarization curves have 2 short transient passivation segments, the first segment undergoes passivation (self-passivation from an active state)/passivity breakdown (transient transpassivation)/pitting corrosion, the second segment undergoes passivation (self-healing)/passivity breakdown (transpassivation)/pitting corrosion irreversibly.

In order to better understand the electrochemical corrosion behavior of the present alloys, cyclic potentiodynamic polarization method was applied in this work. The experimental curves are shown in Fig. 5. Meanwhile, the corresponding electrochemical parameters are listed in Table 3. Cyclic potentiodynamic polarization curves are composed of two main parts, one is a forward sweep (segment 1, a severe potential range from −2.0 V → 2.0 V) and the other is a reverse sweep (segment 2, 2.0 V → −2.0 V). Comparing with the "one way" polarization curves (i.e. only scan in the forward direction), the reverse segment (segment 2) of the cyclic polarization curve occurs in an almost opposite physical process. That is, segments 1 and 2 of a cyclic polarization curves have very the similar electrochemical behaviors but undergo almost the opposite physical processes with changing of the surface state. Consequently, the basic anodic process of the segment 2 curves can be inferred from the above analysis of electrochemical routes of the forward "one way" polarization curves. Several typical parameters such as E_b, E_{pro}, $\triangle E_{p-r}$, $\triangle E_{p-w}$, i_b and i_{corr} are crucial
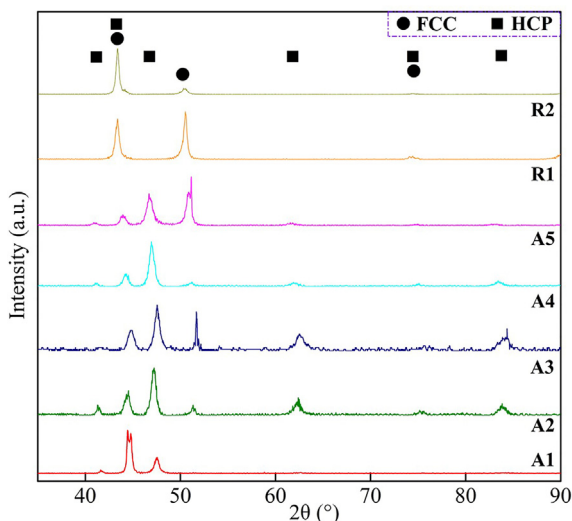

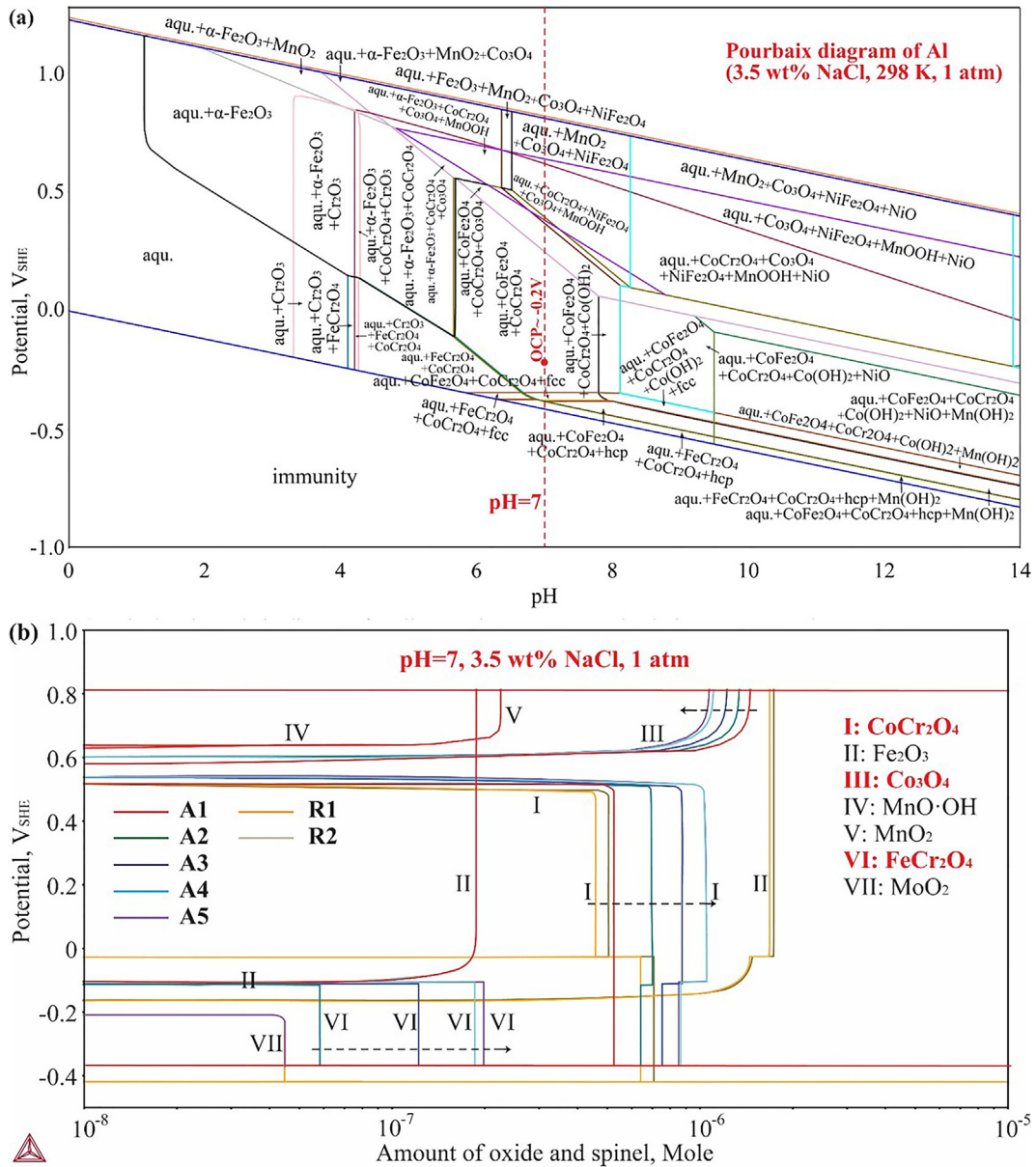**Fig. 2.** XRD patterns of the proposed seven alloys.

Fig. 3. The CALPHAD calculation for predicting corrosion behaviors in 3.5 wt% NaCl solution at 1 atm and room temperature. The Pourbaix diagram (i.e., potential-pH diagram) for A1 alloy (a), the diagram of potential vs the amount of spinel and other oxides for 7 alloys at pH = 7 (b).

for pitting/repassivation and competing processes can be extracted from the corresponding characteristic cyclic potentiodynamic polarization curves. In particular, comparing the actual potential value of a specific metal with E_b and E_{pro}, one can estimate that the metal would probably located in stable or *metastable* pitting corrosion (or crevice corroion) process or in repassivation processes. Since E_{pro} is obtained from the intersection point between the reverse curves (i.e. segment 2) and the curves of passivity region in the forward part (i.e. segment 1), E_{pro} for the alloys A1 to A3 and R2 are not exactly located in the typical passivation state. Meanwhile, alloys A4, A5 and R1 show a typical E_{pro}. In the loop of $E_b \rightarrow 2$ V $\rightarrow E_{pro}$, the alloys undergo a series of complicated processes mainly include passivity breakdown (transient transpassivation)/pitting corrosion irreversibly/repassivation (self-healing), so the smaller of the loop, the higher of the repassivation ability. Particularly, A4 and A5 have very special forward and reverse scan for the cyclic polarization curves. Therefore, alloys A4 and A5 have a very strong repassivation ability for healing from the severe pitting corrosion. This result agrees well with the previous analysis in the polarization curves.

The electrochemical impedance, Z, is the frequency, f, dependent parameter described as follows,

$$Z(f) = \frac{E(f)}{i(f)} = \frac{E_0 \sin(ft)}{i_0(ft + \varphi)} \tag{1}$$

or.

$$Z = Z' + jZ'' = \frac{E_{real} + E_{imaginary}}{i_{real} + ji_{imaginary}} = \frac{E' + jE''}{i' + ji''} \tag{2}$$

where, f is the frequency, φ is the phase angle. Z', E', and i' is the real component of impedance, voltage, and current density, respectively. Z'', E'', and i'' is the imaginary component part. The imaginary component $j = \sqrt{-1}$.

The impedance modulus, $|Z|$, and the phase angle, φ, are show as below,
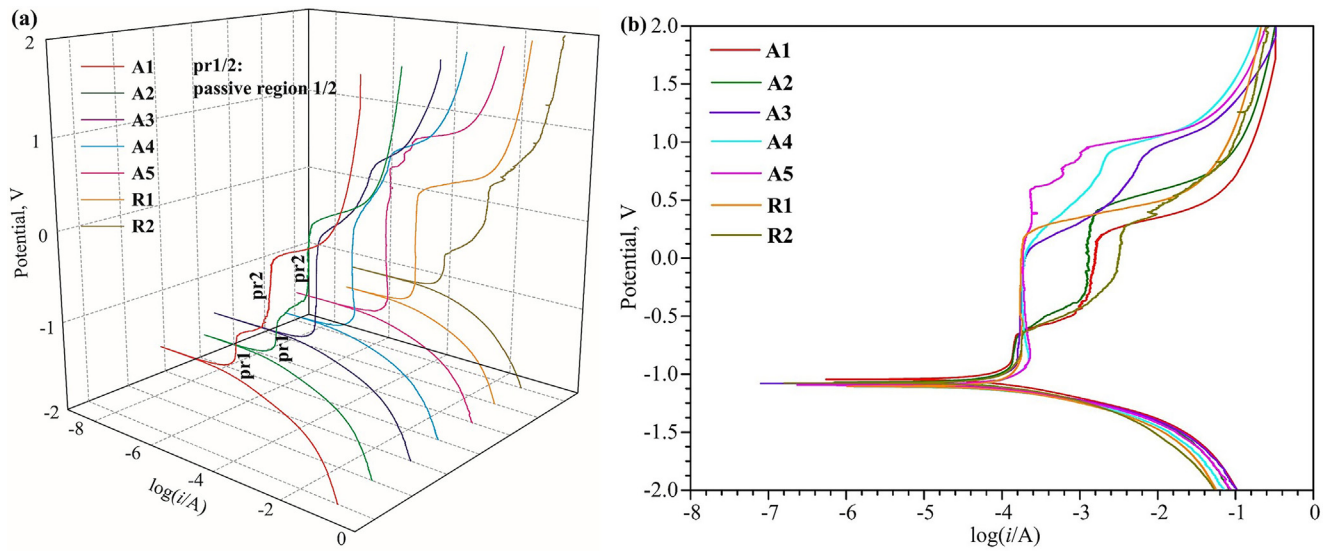
Fig. 4. Polarization curves of the 7 samples in 3.5 wt% NaCl solution at 1 atm and room temperature after 1 h OCP. The polarization curves plotted in two versions: 3D plots (a) and 2D plots (b).

Table 2
The electrochemical parameters analyzed from the polarization curves.

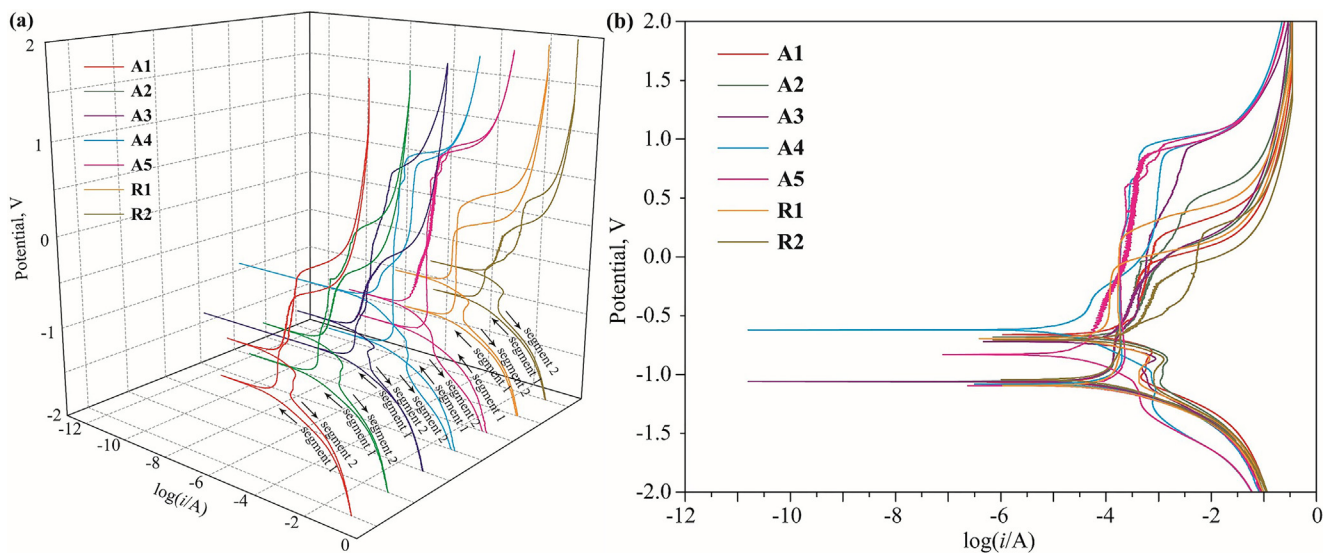| Alloy	β_c, mV/dec	β_a, mV/dec	$\log i_c$	$\log i_a$	R_L, Ω	E_{corr}, V	i_{corr}, μA	i_{corr_auto}, μA	E_b, V	i_b, μA	$\triangle E_{p\text{-}r}$, V	$\triangle E_{p\text{-}w}$, V	E_p, V	i_p, μA	Passivation Segment
A1	120.74	353.61	−4.27	−4.24	543.00	−1.04	55.82	72.04	−0.66	158.31	0.27	0.39	−0.93	116.92	1
	—	—	—	—	—	—	—	—	0.16	1676.10	0.60	1.21	−0.44	996.32	2
A2	117.45	344.83	−4.28	−4.25	531.00	−1.07	55.82	71.69	−0.69	145.88	0.25	0.37	−0.94	127.15	1
	—	—	—	—	—	—	—	—	0.13	968.57	0.61	1.20	−0.48	402.25	2
A3	113.80	313.87	−4.24	−4.25	511.00	−1.08	53.06	68.27	0.01	191.73	0.96	1.09	−0.95	140.35	—
A4	111.71	291.38	−4.15	−4.19	436.00	−1.11	66.44	80.57	−0.01	182.98	0.91	1.10	−0.92	205.49	—
A5	112.08	296.82	−4.23	−4.25	495.00	−1.10	57.28	71.52	0.83	340.96	1.75	1.93	−0.92	171.75	—
R1	121.67	397.14	−4.12	−4.15	409.00	−1.10	73.11	98.94	0.16	182.98	1.08	1.26	−0.92	162.63	—
R2	126.55	387.75	−4.15	−4.19	467.00	−1.07	63.91	88.83	−0.66	176.64	0.23	0.41	−0.89	158.31	—

Fig.5. Cyclic polarization curves of the 7 samples in 3.5 wt% NaCl solution at 1 atm and room temperature after 1 h OCP. The polarization curves plotted in two versions: 3D plots (a) and 2D plots (b). The first and the second half polarization scans are the segment 1 and 2 polarization curves, respectively, the direction of the arrow is the scanning direction. It is worth emphasizing that A4 and A5 have a special characteristic for the two segments of the cyclic polarization curves in comparison with the other 5 samples.

$$|Z|^2 = (Z')^2 + (Z'')^2 \tag{3}$$

$$\tan \varphi = Z''/Z' \tag{4}$$

Fig. 6 shows the EIS experimental data and the corresponding analysis of the 7 samples in 3.5 wt% NaCl solution at 1 atm and room temperature. EIS is a significant technique to study the elec-

Table 3
The electrochemical parameters analyzed from the cyclic polarization curves.

| Alloy	Segment	β_c, mV/dec	β_a, mV/dec	log i	log i_a	R_L, Ω	E_{corr}, V	i_{corr}, μA	$i_{self\text{-}corr}$, μA	E_{pro}, V	i_{pro}, μA	E_b, V	i_b, μA	E_p, V	i_p, μA	$\triangle E_{p\text{-}r}$, V	$\triangle E_{p\text{-}w}$, V
A1	1	115.50	348.92	−4.27	−4.25	529.00	−1.07	55.82	71.27	—	—	0.13	493.95	−0.97	116.92	1.10	1.20
	2	140.55	382.12	−3.98	−3.98	292.00	−0.66	96.92	148.10	−0.07	682.24	−0.11	498.77	−0.54	258.42	0.43	0.55
A2	1	117.56	365.23	−4.23	−4.20	480.00	−1.06	60.58	80.56	—	—	−0.05	454.67	−0.93	134.15	0.88	1.01
	2	135.06	332.01	−3.89	−3.89	253.00	−0.68	127.15	165.10	−0.63	178.30	−0.10	894.75	−0.56	305.56	0.46	0.59
A3	1	114.92	332.89	−4.29	−4.27	548.00	−1.06	51.52	67.74	—	—	0.17	630.96	−0.95	120.23	1.12	1.23
	2	122.87	375.23	−4.09	−4.08	341.00	−0.72	79.74	118.00	−0.22	462.51	−0.27	378.09	−0.60	181.64	0.33	0.45
A4	1	115.94	297.53	−4.20	−4.19	446.00	−1.08	65.72	81.31	—	—	0.62	265.46	−0.93	186.38	1.55	1.70
	2	146.16	219.15	−4.99	−4.99	2868.00	−0.62	10.41	13.29	−0.17	182.95	0.87	1233.67	−0.45	46.82	1.31	1.49
A5	1	115.73	326.16	−4.14	−4.11	420.00	−1.10	75.42	88.49	—	—	0.60	230.52	−0.90	213.85	1.50	1.69
	2	142.03	265.32	−4.74	−4.79	1805.00	−0.83	17.14	22.28	−0.15	180.30	0.82	480.40	−0.61	66.02	1.43	1.65
R1	1	117.22	412.03	−4.11	−4.13	403.00	−1.09	73.11	98.34	—	—	0.13	187.07	−0.89	166.57	1.02	1.22
	2	109.76	372.72	−4.39	−4.31	619.00	−0.70	44.74	59.58	−0.08	171.75	−0.14	127.15	−0.56	104.79	0.41	0.56
R2	1	124.25	357.02	−4.22	−4.23	507.00	−1.04	59.16	79.05	—	—	−0.68	178.65	−0.84	166.57	0.16	0.36
	2	153.59	259.81	−3.79	−3.88	201.00	−0.70	141.87	208.80	−0.67	186.38	−0.25	891.05	−0.55	425.40	0.31	0.45
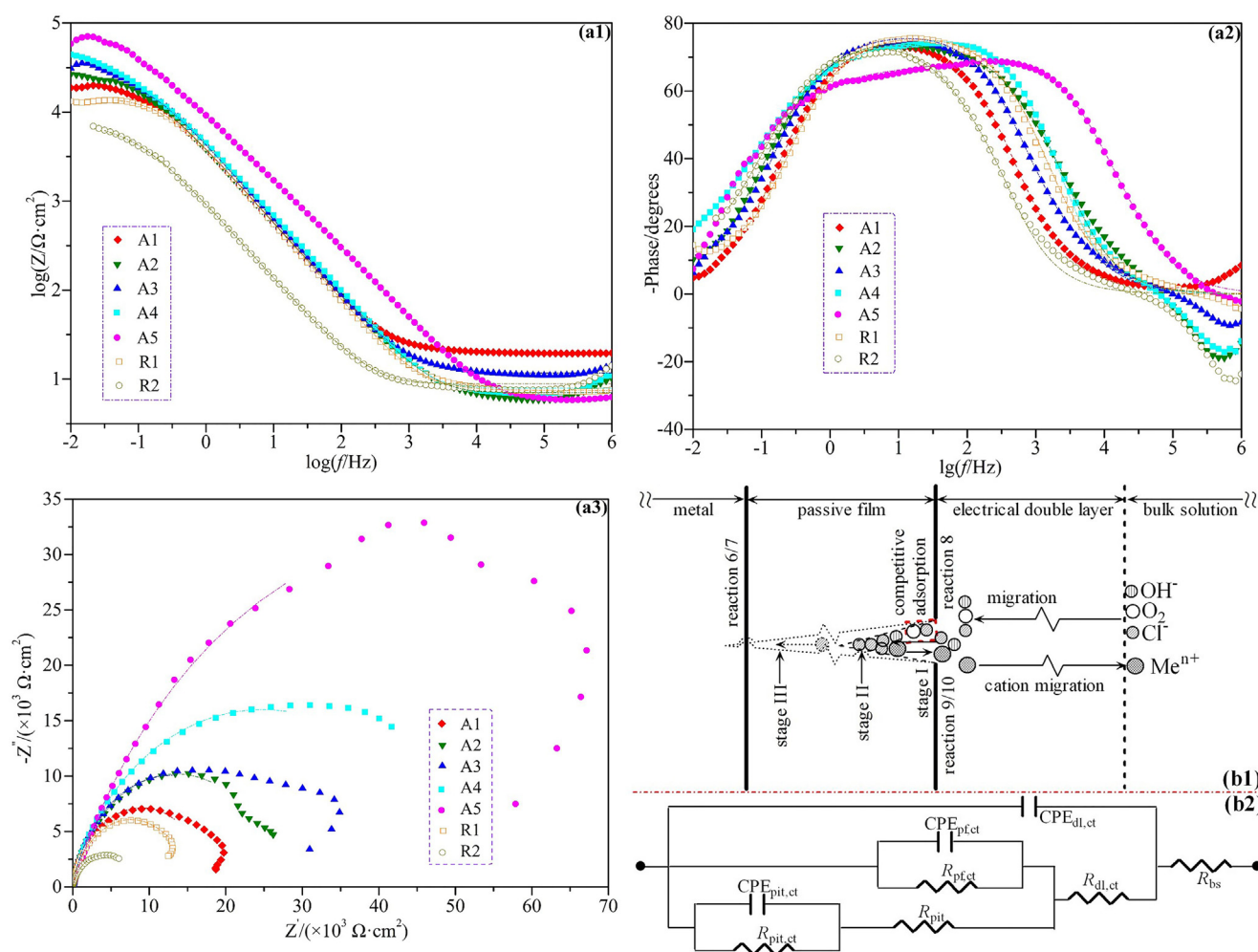
Fig. 6. The EIS experimental data and the corresponding analysis of the 7 samples in 3.5 wt% NaCl solution at 1 atm and room temperature after 1 h OCP. The Bode plots are described by the frequency-dependent impedance modulus (a1) and the phase angle (a2), the Nyquist plots are described by the imaginary versus real component of impedance (a3). By using a diagrammatic sketch of the stability and the breakdown of the passive films (b1), and a simulated equivalent electrical circuit model (b2) to interpret a typical electrochemical interface undergoing the pitting corrosion process in our samples. The dash-dotted curves in Fig. 5 (a1, a2, and a3) are fitted from the simulated electronic components in Fig. 5 (b2). The fitted parameters of the equivalent electrical circuit models are listed in Table 4.

trode/electrolyte interface (i.e. our candidate alloys/NaCl solution in this work), a series of responses of the electrode will be obtained by alternating a series of given disturbance signals (e.g. some electrical parameters) in different frequencies. The EIS is normally plotted in two types on the basis of the excitation & response, i.e.

Bode and Nyquist plots. The Bode plots are shown in Fig. 6(a1 & a2), i.e. the frequency-dependent impedance modulus (Fig. 6(a1)) and the phase angle (Fig. 6(a2)). The Nyquist plots are shown in Fig. 6(a3), i.e. the imaginary versus real component of impedance. Fig. 6(b1) represents a diagrammatic sketch of the stability and the

breakdown of the passive films, Fig. 6(b2) shows an equivalent electrical circuit model, both of them are used to interpret a typical electrochemical interface undergoes pitting corrosion process. The dashed curves in Fig. 6(a1, a2 and a3) are fitted from the simulated electronic components in Fig. 6(b2). The fitted value of the simulated electronic components in the equivalent electrical circuit models is listed in Table 4. The polarization resistance, R_p, represents the overall "resistance force" in the micro-localized corrosion

Table 4
The fitted parameters of the equivalent electrical circuit models for the EIS experimental data.

Alloy	R_{bs}, $\Omega \cdot cm^2$	$CPE_{dl,ct}$, $\times 10^{-6} F/cm^2$	$R_{dl,ct}$, $\Omega \cdot cm^2$	$CPE_{pf,ct}$, $\times 10^{-5} F/cm^2$	$R_{pf,ct}$, $\Omega \cdot cm^2$	R_{pit}, $\times 10^4 \Omega \cdot cm^2$	$CPE_{pit,ct}$, $\times 10^{-5} F/cm^2$	$R_{pit,ct}$, $\times 10^4 \Omega \cdot cm^2$	R_p, $\times 10^4 \Omega \cdot cm^2$	χ^2, $\times 10^{-2}$	ΔG_m, kJ/mol
A1	27.10	17.84	27.10	2.47	4254.00	27.10	1.00	1.86	3.73	3.46	−365.69[a]
A2	7.09	10.03	30.24	3.96	162.30	0.01	0.71	2.80	5.61	2.34	−378.72[a]
A3	11.81	8.92	18.40	1.00	0.01	2256.00	2.97	2.62	5.70	0.45	−389.84[a]
A4	7.93	11.03	17.50	4.00	32.72	0.01	1.00	7.16	14.31	1.77	−405.26[a]
A5	6.12	1.98	39.20	2.56	195.80	0.01	0.15	11.60	23.20	0.12	−411.63[a]
R1	7.43	9.88	15.00	0.81	0.01	130.10	3.50	1.55	3.13	0.09	—
R2	8.90	60.18	21.35	17.52	5.36	7457.00	573.10	0.10	1.68	3.46	—

[a] Gibbs energy change per mole of metal atoms upon increasing oxygen partial pressure from zero to 0.2 at 500 K.
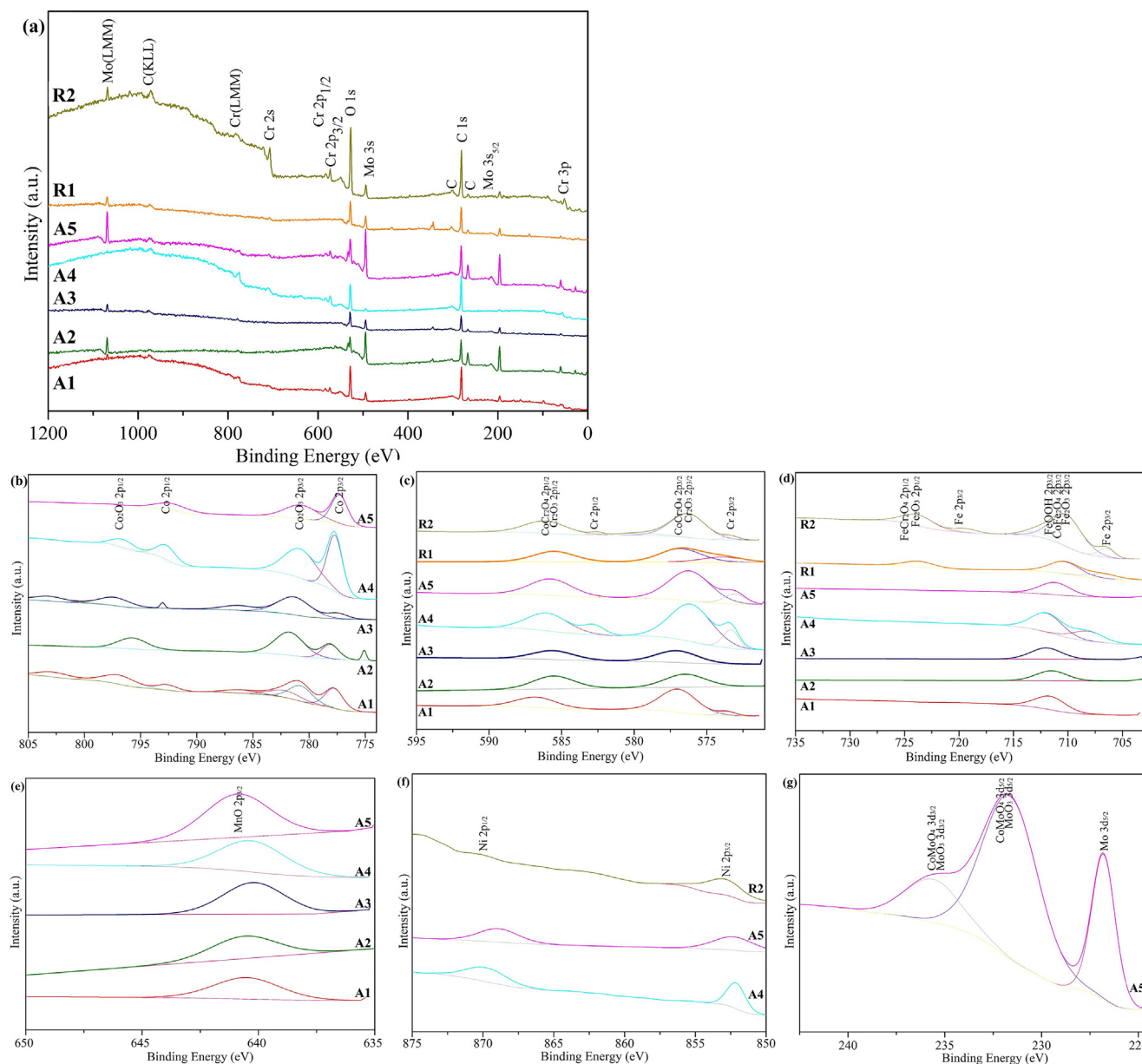

Fig. 7. The XPS survey spectra (a) and high resolution XPS spectra (Co (b); Cr (c); Fe (d); Mn (e); Ni (f); Mo (g)) of the passive films formed on the 7 samples in 3.5 wt% NaCl solution at 1 atm and room temperature for 2 h.

process. R_p was determined by the electrochemical impedance methods, and was then calculated by the Eq. (5) in the present work. Differing from other methods for determining polarization resistance like time domain methods and linear polarization method, the electrochemical impedance methods for determination of polarization resistance is conducted in the frequency domain. Some common errors for the polarization resistance method can be produced, e.g. (1) besides the corrosion behaviors of the determined alloys also probably contain other redox processes in the electrochemical testing system to disturb the results; (2) some experimental parameters maybe influence the results, such as the scan rate of voltage signal; (3) the fluctuation of the instantaneous current and potential in the testing duration; etc. The theoretical error in the measurement of polarization resistance by electrochemical impedance methods can be explained from the simulated electronic components in the equivalent electrical circuit models. Chi-squared values, χ^2, were obtained as shown in the last second column in Table 4.

$$R_p = \frac{R_{pf,ct}(R_{pit,ct} + R_{pit})}{R_{pf,ct} + R_{pit,ct} + R_{pit}} + R_{dl,ct} + R_{bs} \qquad (5)$$

So for the strong corrosion resistance samples, A4 and A5 alloys have a bigger "resistance force" in pitting corrosion, i.e. a bigger value for R_p. A simplified breakdown mechanism for the passive films in the NaCl solution is show in Fig. 6(b1), with some electrode reactions as below.
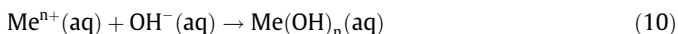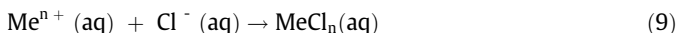
When the passive films breakdown, the typical anodic reactions for the metal matrix are.

$$Me \rightarrow Me^{n+} + ne^- \qquad (6)$$

$$Me \rightarrow Me^{n+}(aq) + ne^- \qquad (7)$$

A typical cathodic reaction is.

$$O_2 + 2H_2O + 4e^- \rightarrow 4OH^- \qquad (8)$$

A pair of competitive overall reactions is.

$$Me^{n+}(aq) + Cl^-(aq) \rightarrow MeCl_n(aq) \qquad (9)$$

$$Me^{n+}(aq) + OH^-(aq) \rightarrow Me(OH)_n(aq) \qquad (10)$$

There are two important theories of passivity, namely "adsorption theory" (also named "chemisorbed film theory") and "diffusion-barrier layer theory" (also named "oxide-film theory") [50], which are particularly suitable for iron-/cobalt-/nickel-based passivation materials [50,51,64–67]. The two major periods of the pitting corrosion usually occur to comply with the two relevant theories. The first period of pitting corrosion is the initiation stage (viz. the pit nucleation stage) which follows the penetration mechanism. The most important behaviors in this period are the competitive adsorption between atomic oxygen (O_{ads}) and chloride ion (Cl^-), the simplified reactions can be found in reactions (6–10). The adsorption of O_{ads} and Cl_{ads} play on two main roles, i.e. as a typical anodic passivator and aggressive ion, respectively. As a typical aggressive anion, Cl^- has a higher adsorption ability to gather and to displace O_{ads} on the surface of the passive film, especially tending to gather on some active site, such as non-metallic inclusions, segregation, intergranular, etc. Compared with other aggressive anions (e.g. SO_4^{2-}), Cl^- penetrates through the passive film at these active sites much easier. The second period is pit propagation stage which obeys the film-breaking mechanism. The most typical behaviors in this period are the autocatalysis process of occluded corrosion battery, i.e. the progressive and stable micro-galvanic corrosion usually in the form of activation-passivation.

4.3. Surface morphologies of the passive films

To investigate the valence state of the passive films formed on the 7 samples in 3.5 wt% NaCl solution at room temperature after 2 h, the XPS survey spectra and high-resolution Co, Cr, Fe, Mn, Ni, Mo XPS spectra were characterized. The results are shown in Fig. 7 (a) to (g). It is necessary to conduct a "charge shift" for the XPS spectra of the elements in alloys based on the binding energy discrepancy of C1s between the standard peak value of 284.8 eV and the experimental data before fitting and analyzing the peaks. The reference binding energies of the 6 elements in the alloys from XPS spectra are listed in Table 5, which is collected from the standard reference database [68,69]. The valence state of the elements and the existed oxides on the passive films were also marked in Fig. 7. No Ni-oxide was formed in the passive films as shown in Fig. 7(f). We will also find the corresponding explanation from the calculated Pourbaix diagram, as shown in Fig. 3, and the OCP experiment. The experimental data of OCP is in the range of about −0.75 to −0.2 V for all the alloys in our study. The 3.5 wt% NaCl solution can be treated as a typical neutral medium, i.e. pH = 7. The OCP cannot be used directly in the Pourbaix diagram, because the potential in the Pourbaix diagram and the OCP are not the same as the description above for the equilibrium and non-equilibrium potential. But the OCP still can be treated as a given potential, which undergoes polarizing from the equilibrium potential, to analyze the Pourbaix diagram. In Fig. 7(f), Ni(II)-oxides appeared with the potential increase over ∼ 0.4 V at pH 7. Therefore, Ni element in the alloys has not achieved the oxidation potential (< ∼0.4 V) under the experimental conditions (as shown in Fig. 3(a)), thus Ni-oxides were not observed in the passive films (as shown in Fig. 7(f)). Besides Ni(II)-oxides, based on some preliminary investigations such as cyclic voltammetry, capacitance and Mott-Schottky, Ni(II)-hydroixde (e.g. α- and β-Ni(OH)$_2$) also need a relatively high initiating potential (∼0.23 V) to be formed at room temperature [70]. The intensities of the peaks in XPS spectra represent the relative amount of the corresponding matters. The results show that there are more Cr_2O_3 and $CoCr_2O_4$ in the passive films formed on alloys A4 and A5 as expected with an increasing Cr content in

Table 5
Binding energies of elements in the alloys from XPS spectra.

Elements	Compound	Binding energy, eV
Co	Co 2p$_{3/2}$/Co 2p$_{1/2}$	777.9/792.95
	CoO 2p$_{3/2}$/CoO 2p$_{1/2}$	780.9/796.4
	Co$_3$O$_4$ 2p$_{3/2}$/Co$_3$O$_4$ 2p$_{1/2}$	779.5/795.9
	Co$_2$O$_3$ 2p$_{3/2}$/Co$_2$O$_3$ 2p$_{1/2}$	781.3/797.1
	CoCr$_2$O$_4$ 2p$_{3/2}$/CoMn$_2$O$_4$ 2p$_{3/2}$/CoFe$_2$O$_4$ 2p$_{3/2}$	780.2/780.0/779.7
	Co(OH)$_2$ 2p$_{3/2}$/Co(OH)$_2$ 2p$_{1/2}$	782.1/798.0
Cr	Cr 2p$_{3/2}$/Cr 2p$_{1/2}$	574.13/583.5
	Cr$_2$O$_3$ 2p$_{3/2}$/Cr$_2$O$_3$ 2p$_{1/2}$	576.5/586.0
	CrO$_2$ 2p$_{3/2}$/CrO$_3$ 2p$_{3/2}$	575.4/579.6
	CoCr$_2$O$_4$ 2p$_{3/2}$/CoCr$_2$O$_4$ 2p$_{1/2}$	576.4/586.1
	Cr(OH)$_3$ 2p$_{3/2}$/Cr(OH)$_3$ 2p$_{1/2}$	577.4/586.8
Fe	Fe 2p$_{3/2}$/Fe 2p$_{1/2}$	706.8/720.2
	Fe$_2$O$_3$ 2p$_{3/2}$/Fe$_2$O$_3$ 2p$_{1/2}$	710.8/724.0
	Fe$_3$O$_4$ 2p$_{3/2}$/Fe$_3$O$_4$ 2p$_{1/2}$	710.4/723.5
	FeCr$_2$O$_4$ 2p$_{3/2}$/FeCr$_2$O$_4$ 2p$_{1/2}$/CoFe$_2$O$_4$ 2p$_{3/2}$	710.6/725.0/710.8/
	NiFe$_2$O$_4$ 2p$_{3/2}$	710.5
	FeO 2p$_{3/2}$/FeOOH 2p$_{3/2}$/FeOOH 2p$_{1/2}$	709.6/711.5/724.3
Mn	Mn 2p$_{3/2}$/Mn 2p$_{1/2}$	638.8/650.2
	MnO$_2$ 2p$_{3/2}$/MnO$_2$ 2p$_{1/2}$	642.4/653.9
	MnO 2p$_{3/2}$/MnO 2p$_{1/2}$	641.4/653.4
Ni	Ni 2p$_{3/2}$/Ni 2p$_{1/2}$	852.8/870.0
	NiO 2p$_{3/2}$/NiO 2p$_{1/2}$	854.4/871.8
	NiFe$_2$O$_4$ 2p$_{3/2}$/NiMn$_2$O$_4$ 2p$_{3/2}$/NiMo$_2$O$_4$ 2p$_{3/2}$	855.4/855.2/856.0
Mo	Mo 3d$_{5/2}$/Mo 3d$_{3/2}$	227.5/231.1
	MoO$_3$ 3d$_{5/2}$/MoO$_3$ 3d$_{3/2}$	232.5/235.8
	MoO$_2$ 3d$_{5/2}$/MoO$_2$ 3d$_{3/2}$	229.3/232.8
	CrMoO4 3d$_{5/2}$/CoMoO4 3d$_{5/2}$/CoMoO4 3d$_{3/2}$	232.2/232.4/235.9

these alloys. MoO$_3$ is present in the passive films for alloy A5. Combining the CALPHAD-predicted Pourbaix diagram (Fig. 3) and the XPS investigations (Fig. 7), it is reasonable to postulate that Cr$_2$O$_3$, CoCr$_2$O$_4$ and MoO$_3$ have increased the mechanical isolation effect of the passive films. Meanwhile, $\Delta G_{m,Ax}$ (Ax = A1 to A5) of spinels and oxides in alloy Ax, Gibbs energy change per mole of metal atoms, was also calculated upon increasing oxygen partial pressure from 0 to 0.2 at 500 K, as listed in the last column in Table 4. From the thermodynamic perspective, the spinels and oxides formed on the surface of the metal matrix will be in a more stable state with the decreasing of $\Delta G_{m,Ax}$. Therefore, calculated $\Delta G_{m,Ax}$ also supports the results from the calculated Pourbaix diagram (Fig. 3) and the XPS investigations (Fig. 7).

The surface roughness has a strong correlation with the corrosion resistance performance of a passivation material. Subsequently, the characterization using an atomic force microscope (AFM) was performed to characterize the surface topography of the passive films to visualize the surface morphology. AFM topographic images of the passive films formed on the alloys in 3.5 wt% NaCl solution at 1 atm and room temperature for 2 h were performed in this work (see Fig. 8). AFM topographic images were adopted in 2 types, one is 3D height morphology (Fig. 8(a1) to (g1)), the other is the phase map (Fig. 8(a2) to (g2)). The depth curves of the corresponding 3D height morphology along the diagonal line from left to right are shown in Fig. 8(h). Each alloy was scanned in 3 to 5 areas to get more typical surface morphologies, and each area was taken by a height morphology and a phase

map. As discussed in the section for polarization and cyclic polarization experiments, the passive films for AFM underwent a comprehensive process, including passivation, depassivation, and repassivation, etc. There exists a complex competition relationship between passivation, depassivation, and repassivation. For micro-localized corrosion, such as pitting corrosion and intergranular corrosion and so on, sensitized regions of the anodic dissolution (i.e. the micro anode) are typically located at inclusions [71], phase/-grain boundaries, damage area of passive films, dislocation outcrop or segregation region, and so on. The surface morphologies during the corrosion process are an intuitive appearance which results from the above factors, like the pitting corrosion (e.g. alloys A1 and A2), and the slip band corrosion (e.g. alloys A3 and R2). The AFM morphology indicate that alloy A5 has the smoothest surface, see Fig. 8(e), although there still exist slight pitting and slip band corrosions. For pitting corrosion, as one of the most representative localized corrosions without stress, the adsorbed and penetrated corrosive anions (Cl$^-$ here) will prone to breakdown the passive films with less Cr$_2$O$_3$, like the plug-type selective corrosion, see Fig. 8(a) and (b). For slip band corrosion, the propagation of the localized anodic dissolution in the form of cleavage and quasi-cleavage mainly results from the microstructure (e.g. the fcc → hcp martensitic phase transformation in the present work), the dislocation slip, the nucleation sites during solidification, and the micro-propagation threshold of the passive films, etc., similar as that for the band-type selective corrosion, see Fig. 8(c) and (g). For example, the dislocation slip bands in the most close-packed
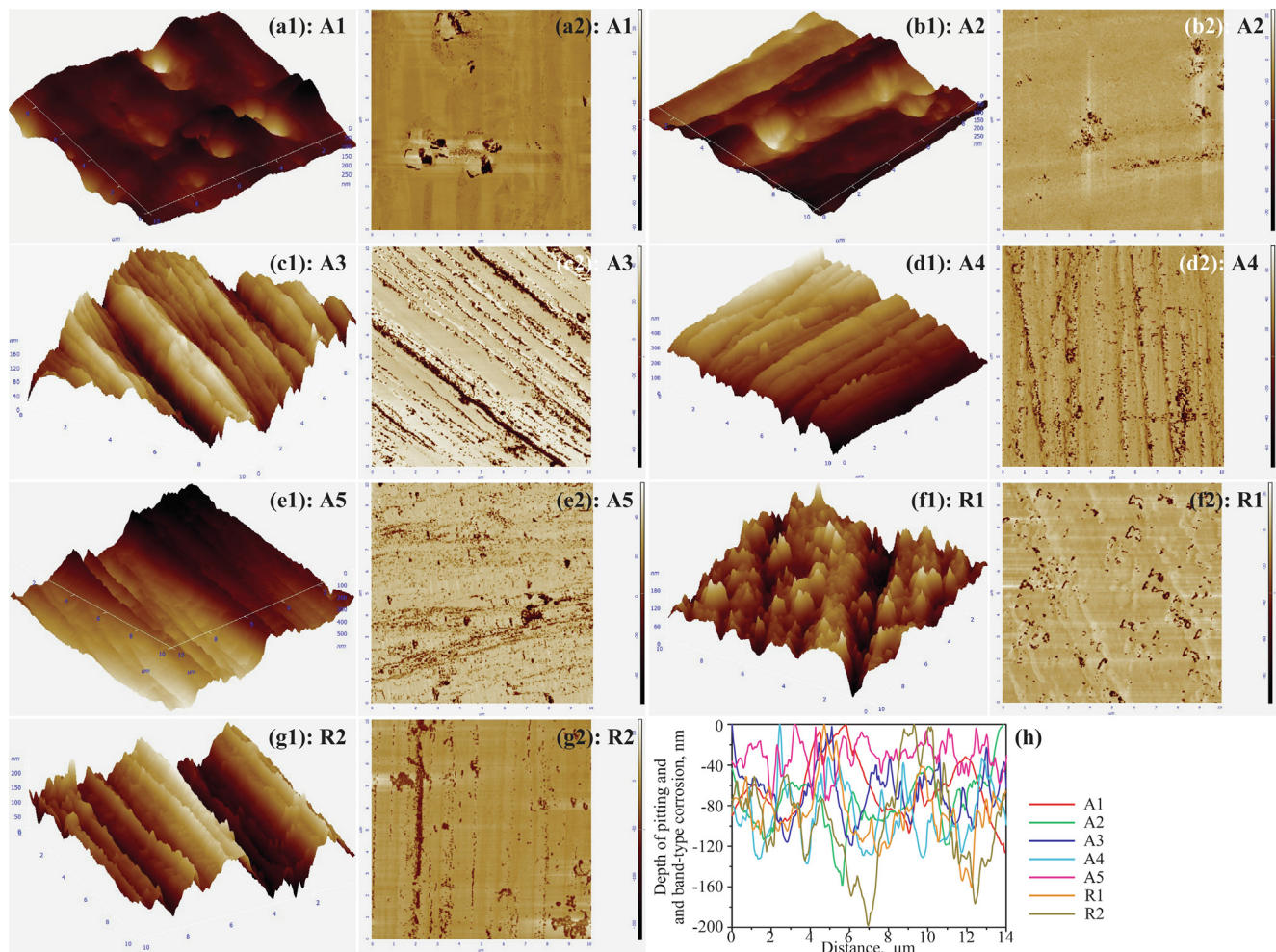

Fig. 8. AFM topographic images of the passive films formed on the 7 samples in 3.5 wt% NaCl solution at 1 atm and room temperature for 2 h. The 3D height morphology ((a1) to (g1)), the phase map ((a2) to (g2)). The depth curves of the corresponding 3D height morphology along the diagonal line from left to right (h).

plane {1 1 1} and the most famous crystallographic orientation a/6 ⟨1 1 2⟩{1 1 1} in fcc crystals [72]. On the other hand, the dislocation slip behaviors are very important factors for the fcc → hcp martensitic phase transformation for the designed duplex fcc + hcp Co-based entropic alloys.

5. Summary

In this work, a series of high corrosion resistance duplex fcc + hcp Co-based entropic alloys have been studied based on various thermodynamic calculations and experimental techniques. The designed alloys with the structures of thermal-induced hcp martensite phase and fcc matrix phase are a kind of particular materials to overcome the typical strength-ductility trade-off mechanical performances. Two of the designed alloys, i.e. Co$_{47.5}$-Cr$_{30}$Mn$_{7.5}$Fe$_{7.5}$Ni$_{7.5}$ and Co$_{46}$Cr$_{30}$Mn$_{7.5}$Fe$_{7.5}$Ni$_{7.5}$Mo$_{1.5}$, have shown the highest corrosion resistance, including high passivation and repasssivation ability. The CALPHAD-predicted Pourbaix diagram was combined with the electrochemical test and XPS investigations to better understand the corrosion mechanism. Ni-oxides were not found in the passive films. The adsorbed and penetrated corrosive Cl$^-$ anions breakdown the passive films of the alloys in two types, i.e. pitting-type and band-type corrosion.

For localized corrosion both with and without stress, the cleavage and quasi-cleavage propagation of the localized anodic dissolution results from the lattice structures as well as the dislocation slip bands for the duplex fcc + hcp Co-based entropic alloys. The martensitic phase transformation and the cleavage and quasi-cleavage type localized anodic dissolution on the basis of dislocation slip theories is worth to be further investigated in the future.

Data availability

Data will be made available on request.

Declaration of Competing Interest

The authors declare that they have no known competing financial interests or personal relationships that could have appeared to influence the work reported in this paper.

Acknowledgements

References

[1] E. Nembach, G. Neite, Precipitation hardening of superalloys by ordered γ'-particles, Prog. Mater. Sci. 29 (3) (1985) 177–319.

[2] W. Wang, H.L. Chen, H. Larsson, H.H. Mao, Thermodynamic constitution of the Al–Cu–Ni system modeled by CALPHAD and ab initio methodology for designing high entropy alloys, Calphad 65 (2019) 346–369.

[3] D. Wei, X. Bai, C. Guo, C. Li, Z. Du, Experimental investigation of isothermal sections at 1373 and 1473 K in the Co–Nb–Ti system, J. Alloys Compd. 870 (2021) 159406.

[4] P.S. Jadhav, C.P. Mohanty, T.K. Hotta, M. Gupta, An optimal approach for improving the machinability of Nimonic C-263 superalloy during cryogenic assisted turning, J. Manuf. Processes 58 (2020) 693–705.

[5] S. Sanchez, P. Smith, Z. Xu, G. Gaspard, C.J. Hyde, W.W. Wits, I.A. Ashcroft, H. Chen, A.T. Clare, Powder bed fusion of nickel-based superalloys: a review, Int. J. Mach. Tools Manuf. 165 (2021) 103729.

[6] D.G. Thakur, B. Ramamoorthy, L. Vijayaraghavan, An experimental analysis of effective high speed turning of superalloy Inconel 718, J. Mater. Sci. 44 (12) (2009) 3296–3304.

[7] D. Dudzinski, A. Devillez, A. Moufki, D. Larrouquère, V. Zerrouki, J. Vigneau, A review of developments towards dry and high speed machining of Inconel 718 alloy, Int. J. Mach. Tools Manuf. 44 (4) (2004) 439–456.

[8] B. Sreenu, R. Sarkar, S.S.S. Kumar, S. Chatterjee, G.A. Rao, Microstructure and mechanical behaviour of an advanced powder metallurgy nickel base superalloy processed through hot isostatic pressing route for aerospace applications, Mater. Sci. Eng. A 797 (2020) 140254.

[9] E.O. Ezugwu, Key improvements in the machining of difficult-to-cut aerospace superalloys, Int. J. Mach. Tools Manuf. 45 (12-13) (2005) 1353–1367.

[10] T. Dharini, P. Kuppusami, P. Panda, R. Ramaseshan, A.M.K. Kirubaharan, Nanomechanical behaviour of Ni–YSZ nanocomposite coatings on superalloy 690 as diffusion barrier coatings for nuclear applications, Ceram. Int. 46 (15) (2020) 24183–24193.

[11] T. Baldridge, G. Poling, E. Foroozmehr, R. Kovacevic, T. Metz, V. Kadekar, M.C. Gupta, Laser cladding of Inconel 690 on Inconel 600 superalloy for corrosion protection in nuclear applications, Optics and Lasers in Engineering 51 (2) (2013) 180–184.

[12] Z. Zhang, D.E.J. Armstrong, P.S. Grant, The effects of irradiation on CrMnFeCoNi high-entropy alloy and its derivatives, Prog. Mater Sci. 123 (2022) 100807.

[13] L.E. Falqueto, D.J. Butkus, J.D.B. De Mello, A.C. Bozzi, C. Scandian, Sliding wear of cobalt-based alloys used in rolling seamless tubes, Wear 376–377 (2017) 1739–1746.

[14] A. Dreano, S. Fouvry, G. Guillonneau, A combined friction energy and tribo-oxidation formulation to describe the high temperature fretting wear response of a cobalt-based alloy, Wear 426–427 (2019) 712–724.

[15] J.W. Wen, H.Y. Che, R. Cao, H. Dong, Y.X. Ye, H.Y. Zhang, J. Brechtl, Y.F. Gao, P.K. Liaw, Evolution of the mechanical properties of a cobalt-based alloy under thermal shocks, Mater. Des. 188 (2020) 108425–108432.

[16] J.W. Yeh, S.K. Chen, S.J. Lin, J.Y. Gan, T.S. Chin, T.T. Shun, C.H. Tsau, S.Y. Chang, Nanostructured high-entropy alloys with multiple principal elements: novel alloy design concepts and outcomes, Adv. Eng. Mater. 6 (2004) 299–303.

[17] B. Cantor, I.T.H. Chang, P. Knight, A.J.B. Vincent, Microstructural development in equiatomic multi-component alloys, Mater. Sci. Eng. A 375–377 (2004) 213–218.

[18] P.-K. Huang, J.-W. Yeh, T.-T. Shun, S.-K. Chen, Multi-principal-element alloys with improved oxidation and wear resistance for thermal spray coating, Adv. Eng. Mater. 6 (12) (2004) 74–78.

[19] S. Gorsse, D.B. Miracle, O.N. Senkov, Mapping the world of complex concentrated alloys, Acta Mater. 135 (2017) 177–187.

[20] Y. Zhang, T.T. Zuo, Z. Tang, M.C. Gao, K.A. Dahmen, P.K. Liaw, Z.P. Lu, Microstructures and properties of high-entropy alloys, Prog. Mater. Sci. 61 (2014) 1–93.

[21] B. Cantor, Multicomponent high-entropy Cantor alloys, Prog. Mater Sci. 120 (2021) 100754.

[22] J.L. Cann, A. De Luca, D.C. Dunand, D. Dye, D.B. Miracle, H. Seok Oh, E.A. Olivetti, T.M. Pollock, W.J. Poole, R. Yang, C. Cem Tasan, Sustainability through alloy design: challenges and opportunities, Prog. Mater Sci. 117 (2021) 100722.

[23] D.B. Miracle, O.N. Senkov, A critical review of high entropy alloys and related concepts, Acta Mater. 122 (2017) 448–511.

[24] Z. Li, K.G. Pradeep, Y. Deng, D. Raabe, C.C. Tasan, Metastable high-entropy dual-phase alloys overcome the strength–ductility trade-off, Nature 534 (7606) (2016) 227–230.

[25] X. Wu, D. Mayweg, D. Ponge, Z. Li, Microstructure and deformation behavior of two TWIP/TRIP high entropy alloys upon grain refinement, Mater. Sci. Eng., A 802 (2021) 140661.

[26] P. Niu, R. Li, Z. Fan, T. Yuan, Z. Zhang, Additive manufacturing of TRIP-assisted dual-phases Fe$_{50}$Mn$_{30}$Co$_{10}$Cr$_{10}$ high-entropy alloy: Microstructure evolution, mechanical properties and deformation mechanisms, Mater. Sci. Eng., A 814 (2021) 141264.

[27] R. Wei, K. Zhang, L. Chen, Z. Han, T. Wang, C. Chen, J. Jiang, T. Hu, F. Li, Novel Co-free high performance TRIP and TWIP medium-entropy alloys at cryogenic temperatures, J. Mater. Sci. Technol. 57 (2020) 153–158.

[28] M. Bahramyan, R.T. Mousavian, D. Brabazon, Study of the plastic deformation mechanism of TRIP–TWIP high entropy alloys at the atomic level, Int. J. Plast. 127 (2020) 102649.

[29] L. Li, H. Chen, Q. Fang, J. Li, F. Liu, P.K. Liaw, Effects of temperature and strain rate on plastic deformation mechanisms of nanocrystalline high-entropy alloys, Intermetallics 120 (2020) 106741.

[30] W. Wang, Z.Y. Hou, R. Lizárraga, Y. Tian, R.P. Babu, E. Holmström, H.H. Mao, H. Larsson, An experimental and theoretical study of duplex fccþhcp cobalt based entropic alloys, Acta Mater. 176 (2019) 11–18.

[31] W. Wang, W. Mu, Z. Hou, S. Sukenaga, H. Shibata, H. Larsson, H.H. Mao, In-situ real time observation of martensite transformation in duplex fcc+hcp cobalt based entropic alloys, Materialia 14 (2020) 100928.

[32] S.J. Chen, H.S. Oh, B. Gludovatz, S.J. Kim, E.S. Park, Z. Zhang, R.O. Ritchie, Q. Yu, Real-time observations of TRIP-induced ultrahigh strain hardening in a dual-phase CrMnFeCoNi high-entropy alloy, Nat. Commun. 11 (2020) 826–833.

[33] Y.J. Liang, L. Wang, B. Cheng, Q. Wu, T. Cao, Q. Xiao, Y. Xue, G. Sha, Y. Wang, Y. Ren, X. Li, L. Wang, F. Wang, H. Cai, High-content ductile coherent nanoprecipitates achieve ultrastrong high-entropy all1oys, Nat. Commun. 9 (2018) 4063.

[34] R. Feng, C. Zhang, M.C. Gao, Z. Pei, Y. Chen, D. Ma, K. An, J.D. Poplawsky, L. Ouyang, Y. Ren, J.A. Hawk, M. Widom, P.K. Liaw, High-throughput design of high-performance lightweight high-entropy alloys, Nat. Commun. 12 (2021) 4329.

[35] S. Picak, T. Wegener, S.V. Sajadifar, C. Sobrero, J. Richter, H. Kim, T. Niendorf, I. Karaman, On the low-cycle fatigue response of CoCrNiFeMn high entropy alloy with ultra-fine grain structure, Acta Mater. 205 (2021) 116540.

[36] H. Luo, Z. Li, A.M. Mingers, D. Raabe, Corrosion behavior of an equiatomic CoCrFeMnNi high-entropy alloy compared with 304 stainless steel in sulfuric acid solution, Corros. Sci. 134 (2018) 131–139.

[37] L. Wang, D. Mercier, S. Zanna, A. Seyeux, M. Laurent-Brocq, L. Perriere, I. Guillot, P. Marcus, Study of the surface oxides and corrosion behaviour of an equiatomic CoCrFeMnNi high entropy alloy by XPS and ToF-SIMS, Corros. Sci. 167 (2020) 108507.

[38] Z. Han, W. Ren, J. Yang, A. Tian, Y. Du, G. Liu, R. Wei, G. Zhang, Y. Chen, The corrosion behavior of ultra-fine grained CoNiFeCrMn high entropy alloys, J. Alloys Compd. 816 (2020) 152583.

[39] W. Kai, C.C. Li, F.P. Cheng, K.P. Chu, R.T. Huang, L.W. Tsay, J.J. Kai, The oxidation behavior of an equimolar FeCoNiCrMn high-entropy alloy at 950 °C in various oxygen-containing atmospheres, Corros. Sci. 108 (2016) 209–214.

[40] M. Zhang, E.P. George, J.C. Gibeling, Elevated-temperature deformation mechanisms in a CrMnFeCoNi high-entropy alloy, Acta Mater. 218 (2021) 117181.

[41] C.M. Barr, J.E. Nathaniel II, K.A. Unocic, J. Liu, Y. Zhang, Y. Wang, M.L. Taheri, Exploring radiation induced segregation mechanisms at grain boundaries in equiatomic CoCrFeNiMn high entropy alloy under heavy ion irradiation, Scr. Mater. 156 (2018) 80–84.

[42] S. Zhao, Z. Li, C. Zhu, W. Yang, Z. Zhang, D.E.J. Armstrong, P.S. Grant, R.O. Ritchie, M.A. Meyers, Amorphization in extreme deformation of the CrMnFeCoNi high-entropy alloy, Sci. Adv. 7 (2021) eabb3108.

[43] Y. Fu, J. Li, H. Luo, C. Du, X. Li, Recent advances on environmental corrosion behavior and mechanism of high-entropy alloys, J. Mater. Sci. Technol. 80 (2020) 217–233.

[44] Y.L. Chou, J.W. Yeh, H.C. Shih, Effect of inhibitors on the critical pitting temperature of the high-entropy alloy $C_{o1.5}CrFeN_{i1.5}T_{i0.5}M_{o0.1}$, J. Electrochem. Soc. 158 (2011). C246–C251.

[45] K.M. Hsu, S.H. Chen, C.S. Lin, Microstructure and corrosion behavior of FeCrNiCoMn$_x$ (x = 1.0, 0.6, 0.3, 0) high entropy alloys in 0.5 M H_2SO_4, Corros. Sci. 190 (2021) 109694.

[46] Z. Niu, Y. Wang, C. Geng, J. Xu, Y. Wang, Microstructural evolution, mechanical and corrosion behaviors of as-annealed CoCrFeNiMo$_x$ (x = 0, 0.2, 0.5, 0.8, 1) high entropy alloys, J. Alloys Compd. 820 (2020) 153273.

[47] H. Luo, S. Zou, Y.H. Chen, Z. Li, C. Du, X. Li, Influence of carbon on the corrosion behaviour of interstitial equiatomic CoCrFeMnNi high-entropy alloys in a chlorinated concrete solution, Corros. Sci. 163 (2020) 108287.

[48] C.P. Lee, C.C. Chang, Y.Y. Chen, J.W. Yeh, H.C. Shih, Effect of the aluminium content of Al$_x$CrFe$_{1.5}$MnNi$_{0.5}$ high-entropy alloys on the corrosion behaviour in aqueous environments, Corros. Sci. 50 (7) (2008) 2053–2060.

[49] P. Wu, K. Gan, D. Yan, Z. Fu, Z. Li, A non-equiatomic FeNiCoCr high-entropy alloy with excellent anti-corrosion performance and strength-ductility synergy, Corros. Sci. 183 (2021) 109341.

[50] P. Marcus (Ed.), Corrosion Mechanisms in Theory and Practice (second edition, revised and expanded), Marcel Dekker, New York, 2002, p. 120.

[51] D. Du, K. Chen, H. Lu, L. Zhang, X. Shi, X. Xu, P.L. Andresen, Effects of chloride and oxygen on stress corrosion cracking of cold worked 316/316L austenitic stainless steel in high temperature water, Corros. Sci. 110 (2016) 134–142.

[52] M.R. Wenman, K.R. Trethewey, S.E. Jarman, P.R. Chard-Tuckey, A finite-element computational model of chloride-induced transgranular stress-corrosion cracking of austenitic stainless steel, Acta Mater. 56 (16) (2008) 4125–4136.

[53] G.B. Olson, Preface to the viewpoint set on: The Materials Genome, Scr. Mater. 70 (2014) 1–2.

[54] S. Gorsse, F. Tancret, Current and emerging practices of CALPHAD toward the development of high entropy alloys and complex concentrated alloys, Int. J. Mater. Res. 33 (19) (2018) 2899–2923.

[55] J.-O. Andersson, T. Helander, L. Hoglund, P. Shi, B. Sundman, Thermo-Calc & DICTRA, computational tools for materials science, Calphad 26 (2002) 273–312.

[56] Thermo-Calc Software, www.thermocalc.com.

[57] Aqueous Solutions Databases: TCAQ3 database, https://thermocalc.com/products/databases/aqueous-solutions.

[58] Pure Substances Databases: SSUB5 database, https://thermocalc.com/products/databases/general-alloys-and-pure-substances.

[59] H. Mao, H.-L. Chen, Q. Chen, TCHEA1: a thermodynamic database not limited for high entropy alloys, J. Phase Equilibria Diffusion 38 (4) (2017) 353–368.

[60] H. Chen, H. Mao, Q. Chen, Database development and Calphad calculations for high entropy alloys: challenges, strategies, and tips, Mater. Chem. Phys. 210 (2018) 279–290.

[61] Nickel-based superalloys databases for thermodynamic and properties data, Thermo-Calc Software AB.

[62] Nickel-based superalloys databases for kinetic data, Thermo-Calc Software AB.

[63] A.I. Shcherbakov, Theory of dissolution of binary alloys and the Tamman rule, Prot. Met. 41 (1) (2005) 30–35.

[64] Y. Wang, C. Li, Y. Lin, Electronic theoretical strudy of the influence of Cr on corrosion ressistance of Fe–Cr alloy, Acta Metall. Sinica 53 (2017) 622–630.

[65] Z. Du, L. Zou, C. Guo, X. Ren, C. Li, Experimental investigation and thermodynamic description of the Fe–Mo–Zr system, Calphad 74 (2021) 102314.

[66] J. Shi, C. Guo, C. Li, Z. Du, Experimental investigation of phase equilibria in the Co–Hf–Mo system at 1373 and 1223 K, J. Alloys Compd. 895 (2022) 162655.

[67] D. Wei, J. Zhao, C. Guo, C. Li, Z. Du, Experimental determination of isothermal sections of the Hf–Nb–Ni ternary system at 950 and 1100 ℃, Int. J. Mater. Res. 113 (2022) 460–475.

[68] C.D. Wagner, W.M. Riggs, L.E. Davis, J.F. Moulder, G.E. Muilenberg (Eds.), Handbook of X-ray photoelectron spectroscopy, Perkin-Elmer Corporation, Eden Prairie, Minnesota, U.S.A., 1979, pp. 72–105.

[69] NIST X-ray Photoelectron Spectroscopy Database, NIST Standard Reference Database 20, Version 4.1, https://srdata.nist.gov/xps.

[70] J. Katić, M. Metikoš-Huković, R. Peter, M. Petravić, The electronic structure of the α-Ni(OH)$_2$ films: Influence on the production of the high-performance Ni-catalyst surface, J. Power Sources 282 (2015) 421–428.

[71] W. Wang, Y. Wang, W. Mu, J.H. Park, H. Kong, S. Sukenaga, H. Shibata, H. Larrson, H. Mao, Inclusion engineering in Co-based duplex entropic alloys, Mater. Des. 210 (2021) 110097.

[72] D.E. Laughlin, K. Hono (Eds.), Physical Metallurgy (Volume 1 5th edition), Elsevier, Oxford, UK, 2014, p. 1627.